

# A low-cost mockup to simulate robotic laser cutting in nuclear decommissioning

Frederico Fernandes Afonso Silva, Murilo Marques Marinho, and Bruno Vilhena Adorno

**Abstract**—This paper introduces a low-cost experimental mockup to simulate the laser cutting process of containers in nuclear decommissioning. It is composed of a three-axis table supporting a cuboid container with ultraviolet-sensitive faces, a six-degree-of-freedom serial manipulator holding an ultraviolet torch that simulates the laser, and a visual system based on cameras and fiducial markers. The system employs a constrained task-space adaptive motion controller that compensates for inaccurate parameters and eliminates the need to calibrate the system. Furthermore, as the motion controller explicitly accounts for geometric constraints, the robot reactively avoids collisions with obstacles while handling the ultraviolet torch. To enhance tracking of the laser-cutting path, we control the ultraviolet beam, which requires only four degrees of freedom, instead of the full end-effector pose. Experiments show that, despite an initially uncalibrated system, the overall system is capable of tracking different trajectories with an overall mean accuracy of 3.9 (sd 2.5) mm when the end-effector pose is controlled and 2.4 (sd 1.3) mm when the ultraviolet beam is controlled.

## I. INTRODUCTION

In scenarios where human access is restricted, such as nuclear decommission, the use of robots can be essential [1]. Mechanical decontamination techniques, such as metal milling, gridding, and blasting can be used when the contamination is limited to near-surface material [2] and can be automated to reduce human exposure. However, those strategies require the contaminated material to be of specific sizes and geometries to simplify their processing [3].

Laser cutting is a suitable strategy for size reduction of contaminated material [4] and the use of robots minimizes human exposure to radiation and aerosol hazards during the cutting process [1]. However, strict quality standards demand high-precision, which often require system calibration [5]–[7]. Given the varying geometry of the contaminated equipment and the changes in their topologies as they are reduced and material is removed, the system may require multiple recalibrations, especially when deviations from the originally pre-planned cutting path occur [8].

To deal with this problem, we introduce a low-cost experimental mockup, show in Fig. 1, to simulate the laser cutting process of containers in nuclear decommissioning. It is composed of a three-axis table supporting a cuboid box with ultraviolet sensitive faces, a six-DoF serial robotic manipulator

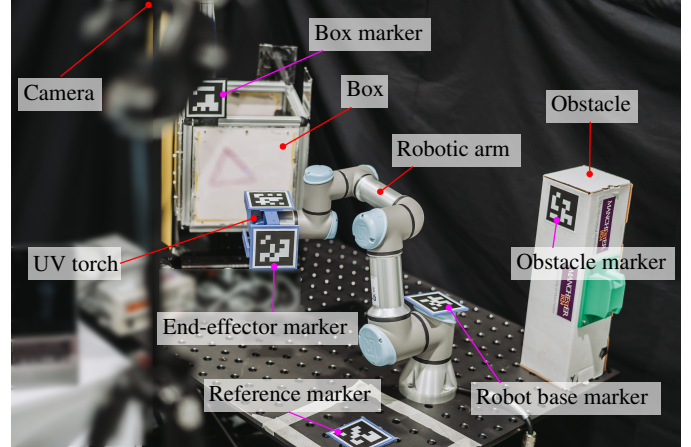


Fig. 1: Low-cost experimental mockup. An Intel RealSense D435i camera obtains the poses of fiducial markers attached to each face of a box mounted on a three-axis table, three markers attached to the robot end-effector to minimize occlusions, as well as markers attached to obstacles, one fiducial marker associated with the robot base, and a reference marker for the world frame.

holding an ultraviolet torch that simulates the laser, and a visual system based on cameras and fiducial markers. The system employs a constrained task-space adaptive motion controller that compensates for inaccurate parameters and eliminates the need to calibrate the system. We use a visual system based on cameras and fiducial markers to provide the adaptive controller with visual measurements to compensate for the uncalibrated geometric parameters, and to track obstacles in the workspace.

### A. Related works

Some solutions for robotic laser cutting in nuclear decommissioning still require intervention from human operators. For instance, Mallion et al. [9] deployed a snake-arm robot to dismantle a dissolver vessel in a contaminated nuclear facility. However, both the robot navigation and the cutting motion were manually performed by an operator by defining and saving waypoints prior to undertaking a cut. Although faster and safer than human missions inside contaminated facilities [10], remotely operated robots are still far from the speed efficiency of automated laser-cutting solutions [3].

Strategies for robotic laser cutting can employ planning in joint or task space. As an example of the former, Ma et al. [11] proposed a path planning algorithm that ensures collision avoidance and satisfy other application-specific constraints for robotic laser cutting in unstructured and cluttered environments. Nonetheless, motion planning in joint space has

F. F. A. Silva, M. M. Marinho, and B. V. Adorno are with the Department of Electrical and Electronic Engineering and the Manchester Centre for Robotics and AI, The University of Manchester, United Kingdom (emails: {frederico.silva; murilo.marinho; bruno.adorno}@manchester.ac.uk).

This work was supported by the Royal Academy of Engineering under the Research Chairs and Senior Research Fellowships programme and the Robotics and AI Collaboration (RAICo).

a computational cost that is exponential in the number of DoFs of the system [12], and, although some solutions allow defining constraints on the end-effector pose [13], defining general task-space constraints can be quite challenging due to the nonlinear mapping between the task-space and the joint-space.

Recent works have focused on planning in the task-space for robotic laser cutting. For instance, Antoš and Bušek [14] presented a solution for the serial production of upholstery products in the automotive industry, which requires the manual design of a trajectory in a simulation environment, whereas Hyun et al. [8] presented a remote dismantling system to be deployed in the decommissioning of nuclear power plants that allows the operator to define high-level task sequences. However, both solutions require the system to be calibrated in advance to represent the actual deployment scenario.

To achieve a solution for robotic laser cutting that eliminates the need for system calibration, enforces safety constraints, is reactive to dynamic changes in the environment, and can track arbitrary task-space trajectories, we employ an adaptive constrained task-space controller [15].

## B. Statement of contributions

This paper presents the following contributions:

- 1) A complete mockup testbed for robotic laser cutting, shown in Fig. (1), that employs ultraviolet beams on a photosensitive box for realistic and safe simulation of the robotic laser cutting process.
- 2) An extension of the adaptive constrained task-space controller proposed in [15] to control the ultraviolet beam instead of the end-effector pose, which releases one degree of freedom (DoF) and increases the robot's functional redundancy with respect to the laser cutting task. This task relaxation is done by controlling a line attached to the end-effector that is always collinear with the ultraviolet beam.

We perform experiments using a UR3e robotic manipulator equipped with an ultraviolet torch, which simulates a laser beam, and a box with photo-sensitive powder, mounted on a bespoke three-DoF table, to mimic the laser-cutting procedure. We then compare the results of following a desired end-effector trajectory with the results of the relaxed task, where the ultraviolet beam is controlled.

## II. ROBOTIC LASER-CUTTING STRATEGY

The proposed architecture for the low-cost experimental mockup to simulate the laser cutting is shown in Fig. 2. The visual system is composed of a Intel RealSense D435 camera and seven fiducial markers to provide the pose information needed for the adaptive controllers to compensate for the uncalibrated geometric parameters of the robot and the box. The path generator system allows the user to define an ordered set  $\mathcal{P}_{UI}$  containing the endpoints of path segments through a graphic user interface (UI). Those endpoints are then scaled and projected onto the box's surface plane, resulting in the set  $\mathcal{P}_b$ . Finally, we perform a linear interpolation between

the initial and final points of each segment in  $\mathcal{P}_b$  to obtain a desired cutting path. Additionally, to help us simulate skips with different surface orientations, the box is placed on top of a moving table with three DoFs that can be controlled through a dedicated UI.

The adaptive control strategy is divided into two optimization problems [15]. The optimal control inputs, given as joint velocities, are obtained as

$$\begin{aligned} \mathbf{u}_q \in \operatorname{argmin}_{\dot{\mathbf{q}}} & \quad \|\mathbf{J}_{\hat{\mathbf{x}},q}\dot{\mathbf{q}} + \eta_q\tilde{\mathbf{x}}\|_2^2 + \|\mathbf{\Lambda}_q\dot{\mathbf{q}}\|_2^2 \\ \text{subject to} & \quad \mathbf{B}_q(\mathbf{q}, \hat{\mathbf{a}})\dot{\mathbf{q}} \preceq \mathbf{b}_q(\mathbf{q}, \hat{\mathbf{a}}) \\ & \quad \mathbf{W}_q(\mathbf{q})\dot{\mathbf{q}} \preceq \mathbf{w}_q(\mathbf{q}), \end{aligned} \quad (1)$$

where  $\dot{\mathbf{q}} \in \mathbb{R}^n$  is the configuration-space velocity vector;  $\eta_q \in (0, \infty)$  is a proportional gain that determines the desired exponential decay rate for the task-space error, and  $\mathbf{\Lambda}_q \in \mathbb{R}^{n \times n}$ , with  $\mathbf{\Lambda}_q > 0$ , is a damping matrix;  $\mathbf{J}_{\hat{\mathbf{x}},q} \in \mathbb{R}^{m \times n}$  is the estimated task Jacobian;  $\tilde{\mathbf{x}} \in \mathbb{R}^m$ , with  $\tilde{\mathbf{x}} = \hat{\mathbf{x}} - \mathbf{x}_d$  is the task error, where  $\hat{\mathbf{x}}$  and  $\mathbf{x}_d$  are the estimated and desired task vectors, respectively;  $\mathbf{B}_q \in \mathbb{R}^{s \times n}$  and  $\mathbf{b}_q \in \mathbb{R}^s$  define  $s$  linear constraints on the control inputs that depend on the estimated parameters,  $\hat{\mathbf{a}} \in \mathbb{R}^p$ ; and  $\mathbf{W}_q \in \mathbb{R}^{s_q \times n}$  and  $\mathbf{w}_q \in \mathbb{R}^{s_q}$  define  $s_q$  linear constraints on the control inputs that are unrelated to the estimated parameters [15].

Then, the optimal adaptation signal, that aims to reduce the error  $\tilde{\mathbf{y}} = \hat{\mathbf{x}} - \mathbf{x}$  between the estimated task-space vector and the measured task-space vector is computed as

$$\begin{aligned} \mathbf{u}_{\hat{\mathbf{a}}} \in \operatorname{argmin}_{\dot{\hat{\mathbf{a}}}} & \quad \left\| \mathbf{J}_{\hat{\mathbf{y}},\hat{\mathbf{a}}}\dot{\hat{\mathbf{a}}} + \eta_{\hat{\mathbf{a}}}\tilde{\mathbf{y}} \right\|_2^2 + \left\| \mathbf{\Lambda}_{\hat{\mathbf{a}}}\dot{\hat{\mathbf{a}}} \right\|_2^2 \\ \text{subject to} & \quad \mathbf{B}_{\hat{\mathbf{a}}}(\mathbf{q}, \hat{\mathbf{a}})\dot{\hat{\mathbf{a}}} \preceq \mathbf{b}_{\hat{\mathbf{a}}}(\mathbf{q}, \hat{\mathbf{a}}) \\ & \quad \mathbf{W}_{\hat{\mathbf{a}}}(\hat{\mathbf{a}})\dot{\hat{\mathbf{a}}} \preceq \mathbf{w}_{\hat{\mathbf{a}}}(\hat{\mathbf{a}}) \\ & \quad \mathbf{N}_{\hat{\mathbf{a}}}\dot{\hat{\mathbf{a}}} = \mathbf{0} \\ & \quad \tilde{\mathbf{x}}^T \mathbf{J}_{\hat{\mathbf{x}},\hat{\mathbf{a}}}\dot{\hat{\mathbf{a}}} \leq 0, \end{aligned} \quad (2)$$

where  $\dot{\hat{\mathbf{a}}} \in \mathbb{R}^p$  is the time derivative of the estimated parameters,  $\eta_{\hat{\mathbf{a}}} \in (0, \infty)$  is a proportional gain that determines the desired exponential decay rate for the estimation error, and  $\mathbf{\Lambda}_{\hat{\mathbf{a}}} \in \mathbb{R}^{p \times p}$ , with  $\mathbf{\Lambda}_{\hat{\mathbf{a}}} > 0$  is a damping matrix;  $\mathbf{J}_{\hat{\mathbf{y}},\hat{\mathbf{a}}} \in \mathbb{R}^{r \times p}$  is the estimated measure-space Jacobian;  $\mathbf{B}_{\hat{\mathbf{a}}} \in \mathbb{R}^{s \times p}$  and  $\mathbf{b}_{\hat{\mathbf{a}}} \in \mathbb{R}^s$  define the linear constraints that depend on the parameters;  $\mathbf{W}_{\hat{\mathbf{a}}} \in \mathbb{R}^{s_{\hat{\mathbf{a}}} \times p}$  and  $\mathbf{w}_{\hat{\mathbf{a}}} \in \mathbb{R}^{s_{\hat{\mathbf{a}}}}$  define  $s_{\hat{\mathbf{a}}}$  linear constraints that are independent of the robot configuration;  $\mathbf{N}_{\hat{\mathbf{a}}} \in \mathbb{R}^{s_{\hat{\mathbf{a}}} \times p}$  is the the parametric task-Jacobian projector that prevents disturbing unmeasured variables; and  $\mathbf{J}_{\hat{\mathbf{x}},\hat{\mathbf{a}}} \in \mathbb{R}^{m \times p}$  is the estimated parametric Jacobian [15].

The adaptive task-space control laws given by (1) and (2) are very general and require a model given in task-space representation. In the present work, the task-space vector can be either a parametrized version of the end-effector pose, such as dual quaternion coefficients, or the coefficients of a line that is collinear to the ultraviolet beam [16]. Nonetheless, any parametrization can be used, as long as the corresponding Jacobian is available.

We use this adaptive control strategy for both the robot and the box to compensate for the uncalibrated geometric parameters across the system. More specifically, the relative

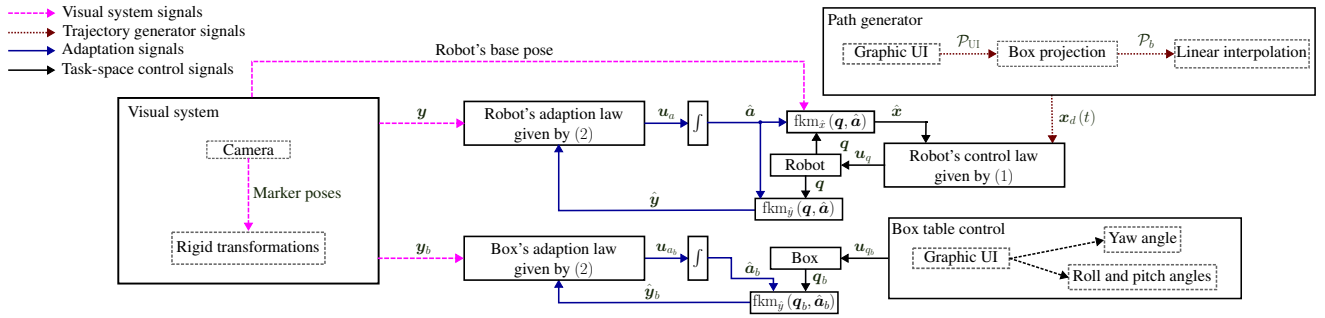


Fig. 2: Mockup architecture. The visual system provides information for the adaptive controller to compensate for the system’s uncalibrated geometric parameters while tracking arbitrary, user-defined task-space paths. Additionally, to simulate skips with different surface orientations, the box is mounted on top of a three-DoF table that can be manually controlled by the user through a graphic UI.

pose between the reference marker and the robot base frame is uncertain, as well as the mechanical attachment of the ultraviolet torch on the end-effector. Furthermore, although the relative pose between the camera and the fiducial markers attached to the skip can be directly measured, the attachment location is inaccurate. Another source of uncertainty is the actual placement of the skip on the bespoke three-DoF moving table, which can be modeled as a spherical joint.

More details about the experimental setup and how the real information is obtained by the system are given in the next sections.

### A. Visual system

We use a visual system based on a Intel RealSense D435 camera and fiducial markers to obtain the pose information needed for the feedback loop in the adaptive law (2), as shown in Fig 2, and for the definition of safety constraints. Namely, we obtain the poses of each fiducial marker with respect to the reference marker from the camera’s API. Then, since there is a physical displacement between each marker and the associated entity to which they relate (see Fig 1), we calculate the nominal (but inaccurate) rigid transformations to retrieve the robot base’s and end-effector’s poses, as well as the poses of the box representing the container and the poses of any possible obstacles in the environment, all with respect to the reference frame. These rigid transformations are inaccurate, in practice, because the mechanical attachments of the fiducial markers are imperfect and contain small positional and orientational errors.

Since the end-effector can be partially occluded during the robot’s motion, we used a 3-D printed device to hold three different markers around the ultraviolet torch. This way, the visual system can use any of them to measure the end-effector pose.

### B. Safety constraints

We use vector field inequalities (VFIs) [17] to enforce hard constraints based on the geometry of the workspace. Each pair of geometric primitives has an associated VFI that ensure they never intersect, guaranteeing safety. Furthermore, each VFI contribute to one row in  $B_q, W_q, B_{\hat{a}}, W_{\hat{a}}$  and one coefficient in  $b_q, w_q, b_{\hat{a}}, w_{\hat{a}}$ . In general, given the signed

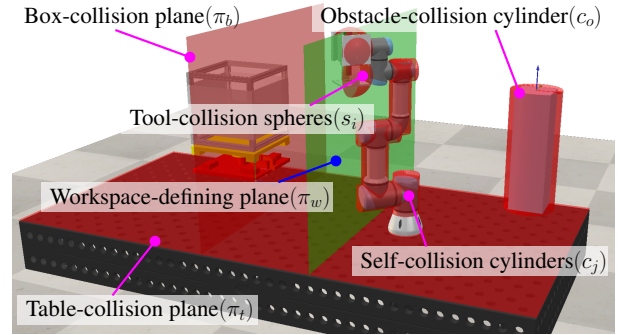


Fig. 3: Digital-twin. Geometric primitives in red indicate zones for the robot’s end-effector to avoid, whereas the green plane indicate the beginning of the operating zone for the end-effector.

distance  $d(g_r(q, \hat{a}), g_w) \in \mathbb{R}$  between a geometric primitive  $g_r(q, \hat{a})$  attached to the robot and a geometric primitive  $g_w$  in the workspace, each VFI in (1) is defined as

$$\underbrace{\frac{\partial d(g_r(q, \hat{a}), g_w)}{\partial q}}_{i\text{th row in } B_q} \dot{q} \leq \underbrace{\eta_{\text{vfi}, q} d(g_r(q, \hat{a}), g_w)}_{i\text{th coefficient in } b_q} \quad (3)$$

when the goal is to keep  $g_r(q, \hat{a})$  outside of  $g_w$ . Conversely, if the goal is to keep  $g_r(q, \hat{a})$  inside  $g_w$ , the corresponding VFI is defined as

$$\frac{\partial d(g_r(q, \hat{a}), g_w)}{\partial q} \dot{q} \leq -\eta_{\text{vfi}, q} d(g_r(q, \hat{a}), g_w). \quad (4)$$

Analogous VFIs with respect to  $\hat{a}$  are used in (2). More details can be found in [15].

The end-effector is tightly enclosed with two spheres  $s_i, i \in \{1, 2\}$  with a radius of 0.075 m, whereas the robot’s links are tightly enclosed with six cylinders  $c_j, j \in \{1, 2, 3, 4, 5, 6\}$  (the first three cylinders have a radius of 0.005 m, the fourth has a radius of 0.045 m and the last two have a radius of 0.04 m), as shown in Fig. 3. Additionally, the obstacle is enclosed with a cylinder  $c_o$  with a radius of 0.1 m, whereas the planes  $\pi_t$  and  $\pi_b$  are used to prevent collisions with the table that supports the robotic manipulator and the box, respectively. Finally, the plane  $\pi_w$  is used to define the beginning of the operating zone for the robot end-effector to operate. As such, there are a total of 19 VFIs (i.e.,  $B_q \in \mathbb{R}^{19 \times 6}$  and  $b_q \in \mathbb{R}^{19}$ ), namely: four VFIs to prevent the collision between the two spheres  $s_1, s_2$

and the two planes  $\pi_t, \pi_b$ ; 12 VFIs for the pair  $(s_i, c_j)$ , for all  $i, j$ , to prevent self-collisions; two VFIs for the pair  $(s_i, c_o)$ , for all  $i$ , to prevent collisions between the end-effector and the obstacle; and one VFI between  $s_1$  and  $\pi_w$  to ensure the end-effector stays within the operating area.

Analogously, there are 19 VFIs associated with the same geometric primitives for the 36 uncertain parameters, namely: all Denavit-Hartenberg parameters (24 in total) and an initial rough estimate of the base frame  $\mathcal{F}_b$  (six) and end-effector frame  $\mathcal{F}_{\text{eff}}$  (six). The transformations  $\mathcal{F}_b$  and  $\mathcal{F}_{\text{eff}}$  are given as six parameters each, representing six sequential transformations. Namely, translations along and three rotations around the  $x$ -axis,  $y$ -axis, and  $z$ -axis, in this respective order. The initial estimations were obtained using a metric tape.

Finally, the joint velocities are limited by defining  $\mathbf{W}_q = \begin{bmatrix} -\mathbf{I}_{6 \times 6} & \mathbf{I}_{6 \times 6} \end{bmatrix}^T$  and  $\mathbf{b}_q = \begin{bmatrix} -\dot{\mathbf{q}}_{\min}^T & \dot{\mathbf{q}}_{\max}^T \end{bmatrix}^T$ .

### C. Task relaxation to control the ultraviolet beam: the line control objective

When laser cutting (or radiating ultraviolet beams), the rotation around the laser axis does not affect the result due to the symmetry of the laser beam. Therefore, controlling the end-effector pose becomes unnecessary. A better approach is to control a line that is collinear with the laser (or ultraviolet) beam so that the rotation around its axis is not controlled, releasing one DoF and creating a functional redundancy with respect to the laser cutting task.

We parametrize the cutting path using lines that are perpendicular to the cutting surface that intersect each point along the path. The control objective is then to make the line that is collinear to the laser/ultraviolet beam converge to the lines along the path. For details on how to obtain the line parameters, the corresponding line Jacobian, and how to calculate the induced distance between lines, refer to [17].

Because the distance between the laser source and the cutting surface affects the cutting quality, the end-effector is constrained to a region that is not too close to the container (too avoid collisions) and not too far (to ensure cutting quality). This region is determined by the red and green vertical planes in Fig. 3.

## III. EXPERIMENTS

We assessed the closed-loop control strategy illustrated in Fig. 2. This way, all the pipeline, including the perception system, path generator, and the adaptive constrained task-space controller can be evaluated in terms of the system's ability to track a desired laser cutting path. We used the computational library DQ Robotics [18] to model the robot and the geometric constraints, as well to implement the control law, all in C++, and the SmartArmStack framework [19] for communication with the robot. We also used CoppeliaSim Edu V4.7.0 [20] as a digital-twin for visualization during the experiments, as shown in Fig 3.

We used a UR3e robotic manipulator, which has six DoF, equipped with a RS PRO LED ultraviolet (UV) torch and a cuboid container to simulate the laser cutting process, as

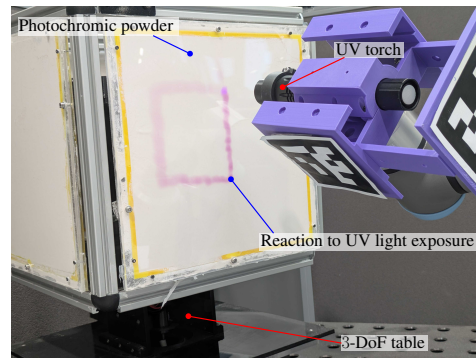


Fig. 4: Cuboid container with ultraviolet sensitive faces. The acrylic surfaces are filled with a photochromic powder that change colors when exposed to UV light.

TABLE I: Parameters for the control law (1) and adaptation law.

$\eta_q$	$\eta_{vfi,q}, \eta_{\hat{a}}, \eta_{vfi,\hat{a}}$	$\Lambda_q$	$\Lambda_{\hat{a}}$	$\dot{\mathbf{q}}_{\min}$ (rad/s)	$\dot{\mathbf{q}}_{\max}$ (rad/s)
50	5	$0.02\mathbf{I}_6$	$0.02\mathbf{I}_{36}$	$-0.2 \cdot \mathbf{1}_6$	$0.2 \cdot \mathbf{1}_6$

shown in Fig. 4. The container has acrylic surfaces filled with a photochromic pigment powder that changes color when exposed to UV light, and is mounted on top of a bespoke table with three independently actuated degrees of freedom. Before each experiment, we rotate the container to simulate the different surfaces orientations that would be present when laser-cutting arbitrary skips.

The parameters used for the experiment are given in Table I.

### A. Definition of cutting paths

Using the procedure described in Section II, we defined four arbitrary cutting paths : a vertical line, a square, a triangle, and a diamond. Those cutting paths were used to generate pose paths for the adaptive controller with pose control objective (ACPO) and line paths for the adaptive controller with line control objective (ACLO).

The pose paths for ACPO are generated as follows. For each point along the cutting path, the end-effector orientation is defined such that its  $z$ -axis is normal and opposite to the box's surface. The end-effector position is defined so that the ultraviolet torch is 15 cm away from the box. For each initial and final point of a given segment in the cutting path, we interpolate the pose path using screw linear interpolation [21] so that both position and orientation change linearly with time.

The line paths for ALPO are defined by assigning a reference line that is perpendicular to the estimated box's surface for each point along the interpolated cutting path, as illustrated in Fig. 5. For both controllers, we enforced the VFIs defined in Section II-B.

Before the robot starts moving, the adaptive control law (2) is run for an arbitrary period of 5s to improve the initial estimated model, which might be very inaccurate due to the lack of calibration. Then, all VFI constraints described in Section II-B are added to the constrained controller, except for the constraint related to the plane  $\pi_w$ , so that the robot end-effector can move to a predefined pose between planes  $\pi_w$  and  $\pi_t$ . Once the end-effector is within the operating area,

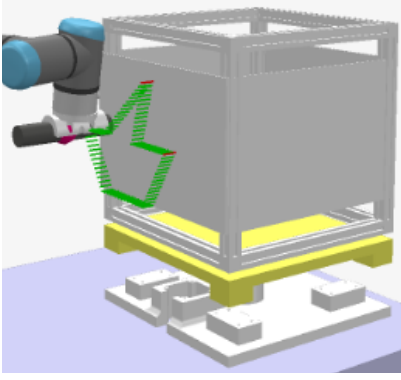


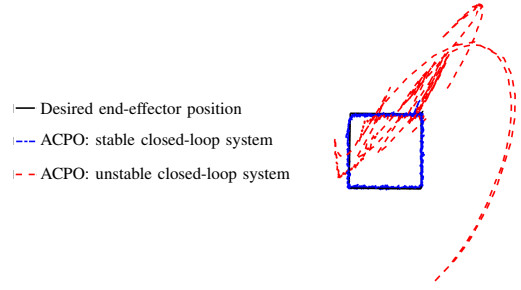
Fig. 5: Line paths for ALPO. Reference lines perpendicular to the box surface are assigned to each point along the interpolated cutting path.

the remaining VFI related to  $\pi_w$  is added to the optimization problem and control laws (1) and (2) are run continuously in a closed-loop so that the desired path is tracked while the robot adapts its uncertain parameters continuously.

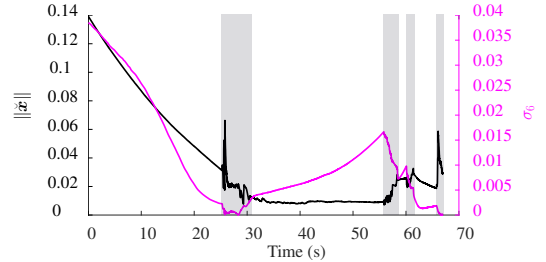
### B. Analysis of the pose control objective

When using the ACPO to track a desired path, there are an infinite number of orientations that keep the ultraviolet torch, which is attached to the end-effector, perpendicular to the box. This is due to the fact that the torch can be continuously rotated around its axis without changing the ultraviolet beam direction. However, due to the constraints of the robot joints and geometric constraints enforced by VFIs, the robot manipulability, which can be measured by the smallest nonzero singular value of the task Jacobian, can change significantly depending on the desired end-effector orientation. This means that the robot might reach configurations near singularities in order to attain the desired end-effector pose while respecting all constraints, which can potentially lead to unstable behavior.

For instance, Fig. 6a shows the UR3e following two desired pose paths: (1) a nominal pose path  $\mathbf{x}_{d_n}(\lambda)$ , with executed path in *blue*, representing a square with the end-effector's  $z$ -axis perpendicular to the surface and the  $x$ - and  $y$ -axes carefully chosen so that the task Jacobian would be well-conditioned at all times; (2) and a modified pose path  $\mathbf{x}_{d_m}(\lambda)$ , with executed path in *red*, in which the end-effector was rotated by  $30^\circ$  about the torch's axis with respect to the nominal desired path. Whereas the closed-loop under ACPO is well behaved when tracking the carefully defined  $\mathbf{x}_{d_n}(\lambda)$ , it tends to become unstable when tracking  $\mathbf{x}_{d_m}(\lambda)$ . This can be explained by inspecting Fig. 6b, which shows the error norm decay and the smallest non-zero singular value of the task Jacobian when tracking  $\mathbf{x}_{d_m}(\lambda)$ . When the smallest singular value decreases substantially or abruptly, the manipulability is affected and the error norm increases substantially. Fig. 6a shows the measured end-effector positions, which are retrieved from the fiducial markers by the visual system. Thus, when the system starts to become unstable, the abrupt pose variations introduce noise spikes into the measurements. This leads to an artificial amplification of the measured end-effector's movement, as shown in Fig. 6a.



(a) Measured positions of the end-effector when using ACPO to track  $\mathbf{x}_{d_n}(\lambda)$  (*blue* curve), which is a pose path with carefully chosen orientations, and  $\mathbf{x}_{d_m}(\lambda)$  (*red* curve), which is a path with the same positions as  $\mathbf{x}_{d_n}(\lambda)$  but with a  $30^\circ$  rotation angle around the end-effector  $z$ -axis. The *solid black* line represents the desired end-effector positions.



(b) Closed-loop error response and smallest non-zero singular value. The norm of the error is given by the dashed black line, whereas the magenta line shows the smallest non-zero singular value of the task Jacobian.

Fig. 6: Effects of different rotation angles around the ultraviolet beam axis, which is collinear with the end-effector  $z$ -axis, when using ACPO to follow paths with the same desired end-effector positions.

Therefore, for a fair comparison between ACPO and ACLO in Section III-C, the desired pose paths for the ACPO, which are defined analogously to  $\mathbf{x}_{d_n}(\lambda)$ , do not take the robot configuration close to singularities.

### C. Comparison of control objectives

Fig. 7 presents the the path traced onto the photosensitive surface when using ACPO and ACLO for the paths detailed in Section III-A. When using ACPO, the executed paths match most sections of the desired ones. However, as shown in Fig. 8 (*black* curve), since the robot is completely actuated with respect to the task of controlling the end-effector pose, any activated constraints will conflict with the tracking task and prevent the error from converging asymptotically to zero. Since we define 20 constraints, 19 being geometric constraints for collision avoidance, at least one of them is activated most of the time. Additionally, as the measurements for the adaptation law are obtained from the camera system using Aruco markers, the noise from those measurements induces fluctuations in the estimated end-effector pose, which explains the high-frequency, low amplitude ( $\sim 1$  mm) oscillation in the time response.

On the other hand, relaxing the task to a line control objective induces a functional redundancy that gives the controller more freedom to minimize the objective function, and hence reduce the tracking error, thereby compensating for activated constraints. As shown in Fig. 8 (*blue* curve), having the

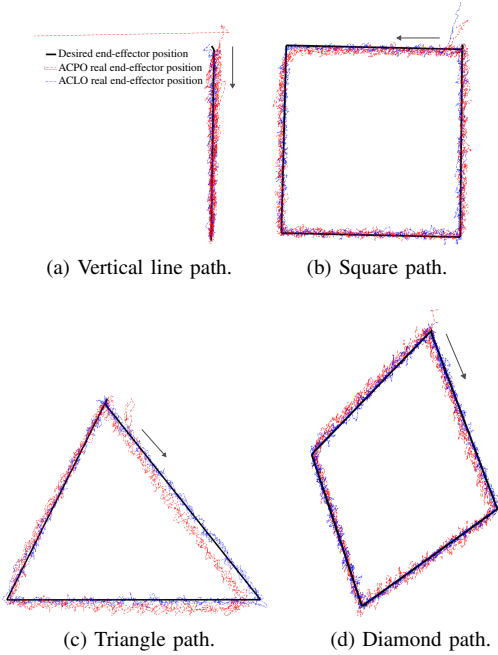


Fig. 7: Traced path while tracking different paths over three of circulations. The solid black line represents the desired path, whereas the red dashed line indicates the traced path when using ACPO, and the blue dot-dashed line shows the traced path when using ACLO. The gray arrows indicate the circulation direction.

TABLE II: Mean accuracy, in mm, of the traced path.

	Vertical line	Square	Triangle	Diamond	Overall
ACPO	3.5 (sd 2.4)	3.2 (sd 1.4)	5.9 (sd 3.4)	3.3 (sd 1.4)	<b>3.9 (sd 2.5)</b>
ACLO	2.6 (sd 1.3)	2.5 (sd 1.5)	2.4 (sd 1.2)	2.1 (sd 1.1)	<b>2.4 (sd 1.3)</b>

flexibility of rotating around and translating along the end-effector ultraviolet beam resulted in a smaller tracking error for all tested paths.

The errors reported in Figs. 7 and 8 show the error norm for tracking poses with ACPO and lines with ACLO. Although from a control standpoint those metrics are fundamental to assess whether the closed-loop system works as intended, they do not provide an easily interpretable quantitative metric for the tracking error because they involve norms in more abstract spaces containing orientations (ACPO) and oriented lines (ACLO). Therefore, even if the ultraviolet beam traced the nominal path accurately, the error norms shown in Fig. 8 might have been affected by larger orientation or line direction errors. Table II summarizes the average accuracy of the *traced path* with respect to the *nominal path*, which is calculated as

$$\text{accuracy} = \frac{1}{T} \int_0^T \|\mathbf{p}_{\text{nom}}(t) - \mathbf{p}_{\text{traced}}(t)\| dt,$$

where  $\mathbf{p}_{\text{nom}}$  and  $\mathbf{p}_{\text{traced}}$  are the nominal and traced path, respectively. Clearly, ACLO renders a much more accurate system.

#### IV. CONCLUSIONS

This paper presented a low-cost mockup for laser-cutting tasks. It consists of a cuboid container with ultraviolet-

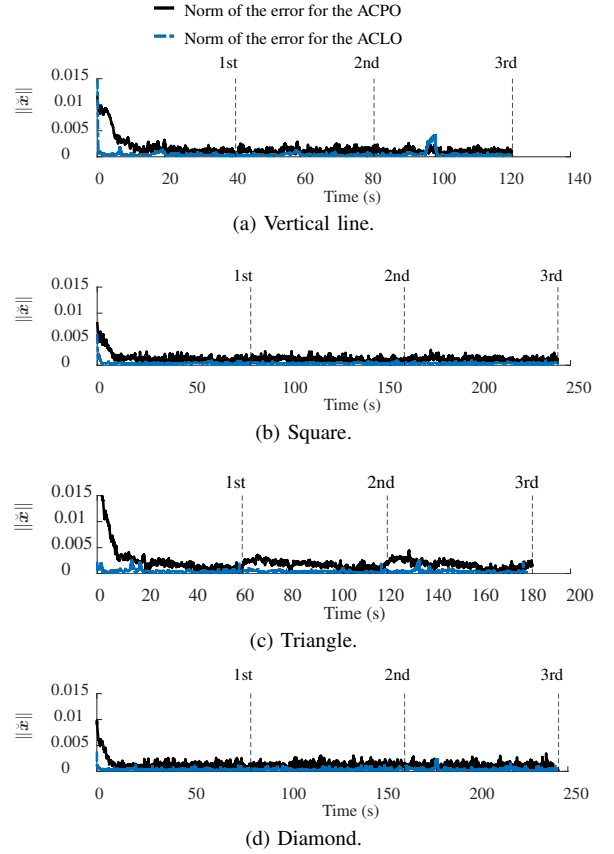


Fig. 8: Norm of the end-effector error while tracking different paths over three of circulations. The solid black line represents the norm of the error for ACPO, while the blue dot-dashed line indicates the norm of the error for ACLO. The vertical dashed lines mark the end of each circulation over the cutting path.

sensitive faces mounted on a three-axis table and a six-DoF robotic manipulator equipped with a UV torch that simulates the laser. The proposed setup uses a visual system based on cameras and fiducial markers to provide an adaptive constrained task-space controller with visual measurements to compensate for inaccurate parameters, eliminating the need to calibrate the system. Furthermore, the robot reactively avoids collisions with obstacles while handling the UV torch since the controller explicitly accounts for geometric constraints.

To enhance the laser-cutting path tracking, we control the ultraviolet beam instead of the full end-effector pose. This reduces the required DoF to perform the task from six to four and induces a functional redundancy that gives the controller more freedom to minimize the objective function. Experimental results have shown that, despite an initially uncalibrated system, the system tracks different trajectories with an overall mean accuracy of 3.9 (sd 2.5) mm when the end-effector pose is controlled and 2.4 (sd 1.3) mm when the ultraviolet beam is controlled.

Future work will focus on replacing the visual perception based on fiducial markers with a markless system based on online 3D reconstruction. We also plan to explore physics-based task sequencing strategies to automate the cut path definition. Lastly, we intend to deploy the laser-cutting system, showcased in the mockup, in actual nuclear decommissioning.

## REFERENCES

- [1] L. C. R. Jones, J. Lavin, A. Cousins, M. Jones, E. J. Long, J. T. Spencer, J. M. Dodds, and J. R. Tyrer, "Laser cutting hazards of nuclear infrastructure decommissioning and dismantling," *Journal of Laser Applications*, vol. 38, no. 1, p. 012010, Feb. 2026.
- [2] M. Lاراia, "Decommissioning of nuclear facilities and environmental remediation: Generation and management of radioactive and other wastes," in *Handbook of Advanced Radioactive Waste Conditioning Technologies*. Elsevier, 2011, pp. 173–204.
- [3] A. Khan, H. Cruickshank, T. Woodcock, I. Pullin, and S. Silverwood, "Laser Size Reduction of Contaminated Magnox Pond Skips–15166," in *WM2015 Proceedings*, Phoenix, Arizona, USA, March 15 – 19, 2015, p. 16.
- [4] P. Hilton and A. Khan, "New Developments in Laser Cutting for Nuclear Decommissioning - 14045," in *WM2014 Proceedings*, Phoenix, Arizona, USA, Mar. 2014, p. 15.
- [5] J. Konecny, P. Beremlijski, M. Bailova, Z. Machacek, J. Koziorek, and M. Prauzek, "Industrial camera model positioned on an effector for automated tool center point calibration," *Sci Rep*, vol. 14, no. 1, p. 323, Jan. 2024.
- [6] J.-X. Liu, T. Chen, Y.-Y. Tsai, and P.-C. Lin, "A Kinematic Parameter Calibration Method of a 6-Axis Industrial Robot Using an Eye-in-Hand 2-D Laser Profiler," *IEEE Sens. Lett.*, vol. 9, no. 7, pp. 1–4, Jul. 2025.
- [7] Y. Yang, P. Zhang, Y. Shi, and Z. Li, "High-Precision and Robust Calibration of the Laser Tool Frame for Industrial Robotic Scribing," in *2025 7th International Conference on Robotics, Intelligent Control and Artificial Intelligence (RICAI)*. Hangzhou, China: IEEE, Nov. 2025, pp. 54–60.
- [8] D. Hyun, I. Kim, S. Joo, J. Ha, and J. Lee, "Remote dismantling system using a digital manufacturing system and workpiece localization for nuclear facility decommissioning," *Annals of Nuclear Energy*, vol. 195, p. 110182, Jan. 2024.
- [9] A. Mallion, C. Wilson, R. Smith, G. Ferguson, R. Roberts, and P. Hilton, "LaserSnake2: An Innovative Approach to Nuclear Decommissioning," in *WM2017 Proceedings*, Phoenix, Arizona, USA, March 5 – 9, 2017, p. 11.
- [10] A. Mallion, C. Wilson, A. Graham, and P. Hilton, "LaserSnake2: Remote High Powered Laser Cutting in Confined Hazardous Spaces," in *WM2016 Proceedings*, Phoenix, Arizona, USA, March 6 – 10, 2016, p. 13.
- [11] S. Ma, S. Zabihifar, and A. Montazeri, "Constrained Motion Planning for Safe Operation of a Vision-Based Laser Cutting Manipulator," in *2024 UKACC 14th International Conference on Control (CONTROL)*. Winchester, United Kingdom: IEEE, Apr. 2024, pp. 84–89.
- [12] S. M. LaValle, *Planning Algorithms*. Cambridge: Cambridge University Press, 2006.
- [13] D. Berenson, S. Srinivasa, and J. Kuffner, "Task Space Regions: A framework for pose-constrained manipulation planning," *The International Journal of Robotics Research*, vol. 30, no. 12, pp. 1435–1460, Oct. 2011.
- [14] J. Antoš and M. Bušek, "Robotic 3D Laser Cutting of Textiles," in *Advances in Mechanism Design IV*, J. Beran, M. Bílek, M. Václavík, and P. Žabka, Eds. Cham: Springer Nature Switzerland, 2024, vol. 171, pp. 167–172.
- [15] M. M. Marinho and B. V. Adorno, "Adaptive Constrained Kinematic Control Using Partial or Complete Task-Space Measurements," *IEEE Trans. Robot.*, vol. 38, no. 6, pp. 3498–3513, Dec. 2022.
- [16] B. V. Adorno, "Robot Kinematic Modeling and Control Based on Dual Quaternion Algebra – Part I: Fundamentals," Tech. Rep., 2017.
- [17] M. M. Marinho, B. V. Adorno, K. Harada, and M. Mitsuishi, "Dynamic Active Constraints for Surgical Robots Using Vector-Field Inequalities," *IEEE Transactions on Robotics*, vol. 35, no. 5, pp. 1166–1185, Oct. 2019.
- [18] B. V. Adorno and M. Marques Marinho, "DQ Robotics: A Library for Robot Modeling and Control," *IEEE Robotics & Automation Magazine*, vol. 28, no. 3, pp. 102–116, Sep. 2021.
- [19] M. M. Marinho, J. J. Quiroz-Omaña, and K. Harada, "A Multiarm Robotic Platform for Scientific Exploration: Its Design, Digital Twins, and Validation," *IEEE Robot. Automat. Mag.*, pp. 2–12, 2024.
- [20] E. Rohmer, S. P. N. Singh, and M. Freese, "V-REP: A versatile and scalable robot simulation framework," in *2013 IEEE/RSJ International Conference on Intelligent Robots and Systems*. IEEE, Nov. 2013, pp. 1321–1326.
- [21] A. Sarker, A. Sinha, and N. Chakraborty, "On Screw Linear Interpolation for Point-to-Point Path Planning," in *2020 IEEE/RSJ International Conference on Intelligent Robots and Systems (IROS)*. Las Vegas, NV, USA: IEEE, Oct. 2020, pp. 9480–9487.